Eurasian Journal of Physics and Functional Materials

2026, 10(2), 103-120

Nanostructuring of Single Crystalline $SnSb_2Te_4$ and $GeBi_2Te_4$ van der Waals Compounds by High-Energy Ball Milling

Kh.Z. Mehtiyeva[1,*], M. Casciaro[2,3], F.K. Aleskerov[4], Kh.M. Ahmadova[5], I.R. Amiraslanov[1], M. Papagno[2,3], Z.S. Aliev[1,6],

[1]Baku State University, Baku, Azerbaijan

[2]Dipartimento di Fisica, Universita della Calabria, Arcavacata di Rende, Cosenza, Italy

[3]Laboratorio di Spettroscopia Avanzata dei Materiali, STAR IR,Via Tito Flavio,Universita della Calabria, Rende, Cosenza, Italy

[4]National Aviation Academy of Azerbaijan, Baku, Azerbaijan

[5]Baku Engineering University, Baku, Azerbaijan

[6]Institute of Physics, Ministry of Science and Education of the Republic of Azerbaijan, Baku, Azerbaijan

E-mail: xatira.mehtiyeva@bsu.edu.az

DOI: **10.32523/ejpfm.2026100201**
Received: 11.03.2026 - after revision

Thermoelectric materials, an important class within the semiconductor family for energy conversion, have been extensively studied in bulk form. However, growing interest in nanoscale materials driven by the quantum confinement effect has made it increasingly important to investigate how their properties change at reduced dimensions. In this work, we demonstrate the successful fabrication of nanosized ternary van der Waals (vdW) compounds $SnSb_2Te_4$ and $GeBi_2Te_4$ from their high-quality single crystals using High Energy Ball Milling (HEBM) for the first time. Here we discuss the effect of milling variables, i.e., materials of the milling container or grinding vessel and balls, milling medium (wet vs. dry), milling time, etc. The scanning electron microscopy with energy-dispersive X-ray spectroscopy (SEM-EDX) analysis of the fabricated nanopowders reveals a strong sensitivity of the samples to the grinding vessel and ball materials, which introduces significant contamination during the milling process. Upon the milling time, this contamination can significantly impact the final composition of the powder, which is undesirable for functional semiconductor materials, where electronic properties are highly sensitive to impurities. Using different types of milling equipment, we demonstrate that nanoscale refinement with

minimal impurity can be achieved simply by selecting appropriate milling materials, without modifying the target material or using protective agents. This result is particularly valuable for the preparation of high-purity nanoscale thermoelectric materials based on single-crystalline layered vdW compounds by the top-down method.

Keywords: van der Waals materials; ternary tellurides; topological insulators; thermoelectrics; nanostructuring; high-energy ball milling

Introduction

Thermoelectric (TE) materials enable the direct conversion of waste heat into electricity, making them valuable for thermoelectric power generation and cooling [1]. The materials efficiency for thermoelectric applications is measured by the thermoelectric figure of merit (ZT), $Z = \sigma S^2 T/\kappa$. For high ZT, the material should combine a high Seebeck coefficient (S) and electrical conductivity (σ) or high-power factor (σS^2) with low thermal conductivity (κ) [2,3]. However, these factors are intrinsically interrelated, complicating simultaneous optimization.

Unlike conventional energy-conversion systems that rely on moving parts or chemical reactions, thermoelectric devices operate through an all-solid-state mechanism that directly converts a temperature gradient into electrical power. This design ensures long-term stability, scalability, and environmental compatibility, enabling applications that range from industrial waste-heat recovery to radioisotope thermoelectric generators (RTGs) used in space exploration [4].

Ternary and more complex chalcogenides of p- and d-metals with long-period crystal structures have attracted increasing attention as prospective thermoelectric materials thanks to their large crystal lattices built up by heavy atoms. Their low thermal conductivity stems from the heavy elements and weak interlayer bonding within large unit-cell dimensions, all of which contribute to strong phonon scattering.

Ternary layered tellurides in the homologous series $n(\mathrm{A^{IV}B^{VI}}) \cdot m(\mathrm{A_2^{V}B_3^{VI}})$ ($\mathrm{A^{IV}} = \mathrm{Ge, Sn, Pb}$; $\mathrm{A^{V}} = \mathrm{Bi, Sb}$; $\mathrm{B^{VI}} = \mathrm{Te}$), and in particular $SnSb_2Te_4$ and $GeBi_2Te_4$, have emerged as promising materials due to their dual thermoelectric and topological functionalities. These compounds combine large atomic masses with vdW interlayer bonding, a combination that reduces lattice thermal conductivity through enhanced phonon scattering while often preserving good carrier mobility. Consequently, strategies that modify microstructure (e.g., nanostructuring), introduce controlled defects, or apply aliovalent substitutions have been shown to tune carrier concentration and phonon transport, leading to improved thermoelectric metrics [5,6].

Since the pioneering work of Dresselhaus and co-workers in the 1990s [7,8], the role of low-dimensional systems and nanostructures has been extensively used to enhance the thermoelectric performance. These insights have driven significant progress in synthesizing nanoscale materials [9–15] and the fabrication of nanocomposites [16,17]. Nanostructuring remains one of the most effective strategies to improve the thermoelectric ZT by reducing lattice thermal conductivity through enhanced phonon scattering while maintaining adequate carrier transport [18]. Among the nanostructuring by top-down methods, HEBM is particularly attractive because it allows fine control over grain size and scalabil-

ity for bulk powder synthesis. It remains a widely adopted method due to its simplicity and scalability, particularly for producing nanoscale BiSbTe powders [13]. However, in the layered vdW compounds, e.g., weak Te(1)–Te(1) bonding between neighboring layers, leads to easy cleavage along the basal plane, which presents additional challenges for large-scale processing of nanoparticles [19,20]. Furthermore, the repeated high-energy impacts during ball milling can cause significant lattice strain, chemical bond breakage, and even partial amorphization or decomposition [21]. Contamination from the milling tools can also affect the intrinsic properties of materials, which can lead to complicated subsequent electrical transport behavior measurements and potentially divert research outcomes. Consequently, researchers continuously seek more sophisticated but less costly top-down approaches to overcome such problems. Therefore, understanding how milling conditions and vessel materials influence structure and purity is crucial.

Here, we report the nanoflake fabrication of $SnSb_2Te_4$ and $GeBi_2Te_4$ single crystals via HEBM. Two different milling systems with distinct grinding vessels were employed: one using tungsten carbide (WC) and the other hardened steel. We investigated the effect of the milling material on the contamination of the nanoflakes, and compared dry and wet milling conditions to evaluate their influence on particle size reduction in both systems. To the best of our knowledge, there has been no any published report to date on the nanoparticle fabrication of ternary vdW compounds belonging to the above-mentioned homologous series.

2. Experimental details

2.1 Growth of bulk single crystals

The single-crystal growth of the $SnSb_2Te_4$ and $GeBi_2Te_4$ compounds was performed in two steps, but under the same conditions for both compounds. First, the polycrystalline compositions were synthesized from high-purity (5N) elements in an evacuated quartz ampoule at approximately 1000 K for 8 hours, with constant mixing, followed by air cooling. Afterwards, the polycrystalline samples were placed in conical-bottom quartz ampoules, which were sealed under a vacuum better than 10^{-4} Pa. At the beginning of the growing process, the ampoules were held in the upper "hot" T_1 zone (~ 950 K) of a two-zone tube furnace for 5 hr. The ampoules then moved from that zone to the "cold" T_2 zone at a rate of 1.0 mm/hr. In this way, bulk ingots of both compounds with average dimensions of ~ 3 cm in length and 0.8 cm in diameter were obtained. The as-grown ingots were examined by Powder X-ray diffraction (PXRD) and confirmed to consist of single-crystalline blocks of $SnSb_2Te_4$ and $GeBi_2Te_4$.

2.2 Milling of $SnSb_2Te_4$ and $GeBi_2Te_4$ bulk crystals

2.2.1. Pre-milling preparation and milling systems

The as-grown $SnSb_2Te_4$ and $GeBi_2Te_4$ bulk single crystals were first manually ground using an agate mortar and pestle. This pre-milling hand-grinding pro-

cess helps to reduce large single crystals into a more homogeneous powder, which is critical since the milling balls cannot efficiently fracture huge fragments. Additionally, the use of an agate mortar minimized the risk of contamination compared to conventional ceramic mortars and grinding large bulk crystals in a bowl, ensuring that no contaminants were introduced before HEBM. For each milling experiment, one gram of hand-ground powder was used, with a fixed ball-to-material weight ratio (BMR) of 10:1.

At first, the single crystalline $SnSb_2Te_4$ pieces were subjected to HEBM using two different systems: the FRITSCH Planetary Mill PULVERISETTE 7 and the FRITSCH Planetary Mill PULVERISETTE 6. The PULVERISETTE 7, a premium-line system with intelligent control, is equipped with two 80 mL tungsten carbide (WC) grinding vessels and balls. The rotational speed of the main disk can be varied between 150 and 1100 rpm, allowing nanometre-scale refinement.

In contrast, the PULVERISETTE 6, a classic-line system, is equipped with one 80 mL stainless-steel grinding vessel and balls, operating at a fixed rotational speed of 650 rpm. These samples were prepared in the systems, hereafter referred to as Sample A (PULVERISETTE 7) and Sample B (PULVERISETTE 6). After optimizing the milling parameters on $SnSb_2Te_4$, the same conditions were successfully applied to $GeBi_2Te_4$ single crystals, resulting in the formation of nanoparticle-sized powders, hereafter referred to as Sample C.

2.2.2 Milling of sample A

Nanoparticles of Sample A were prepared using a FRITSCH Planetary Mill PULVERISETTE 7 milling system equipped with a WC grinding vessel and balls. Milling was performed at a rotational speed of 450 rpm for a total duration of 20 hours. PXRD patterns of the samples were collected every 5 hours. These periodic measurements served to track changes in crystallite size, phase identification, and the progression of amorphization.

Two alternative milling protocols, dry milling and ethanol-assisted wet milling, were employed to investigate the impact of the grinding medium on milling duration and particle size reduction. Notably, the addition of ethanol significantly enhanced the grinding efficiency during both manual pre-treatment and milling. In the milling process, grinding occurs when particles are caught, or "nipped," between colliding grinding balls, leading to fracture and size reduction. In wet milling, a lubricant or surfactant is introduced to minimize cold welding. Ethanol acts as a surface-active agent by adsorbing onto the powder particle surfaces, reducing surface energy and thereby suppressing cold welding and agglomeration. This effect is particularly beneficial for layered materials, as ethanol promotes shear forces and layer cleavage while also limiting static charge buildup and surface oxidation.

2.2.3 Milling of samples B and C

Sample B was prepared under the same conditions using the FRITSCH Planetary Mill PULVERISETTE 6 equipped with a hardened stainless-steel (Fe-Cr) grinding

vessel and balls. The milling duration was extended up to 40 hours to explore the effect of prolonged mechanical treatment. The same protocol was successfully applied to $GeBi_2Te_4$ (Sample C).

2.3. Characterization techniques

2.3.1 Powder X-ray diffraction

PXRD analyses were performed using a Bruker D2 Phaser diffractometer with CuKα radiation ($\lambda = 1.5406$ Å), operating at 30 kV and 10 mA. Diffraction patterns were collected at 5-hour intervals throughout the milling process to monitor the evolution of phase composition, phase stability, and crystallite size reduction. Such step-by-step analyses enabled detailed evaluations of crystallite size reduction, the onset of amorphization, and the possible formation of secondary phases. To estimate the average crystallite size at different stages of the milling process, the well-known Debye–Scherrer equation was employed:

$$D = \frac{K\lambda}{\beta \cos\theta} \tag{1}$$

where D is the mean crystallite size, K is the shape factor (taken as 0.89), λ is the X-ray wavelength (1.5406 Å), β is the full width at half maximum (FWHM) of the selected diffraction peak in radians (corrected for instrumental broadening), and θ is the Bragg angle in radians. Crystallite size was calculated using the most intense and well-isolated diffraction peaks. Before analysis, instrumental broadening was determined using a standard reference material, and all peak widths were corrected accordingly.

2.3.2 Scanning electron microscopy and energy-dispersive X-ray spectroscopy (SEM-EDX)

Microstructural analyses of samples were conducted using a Field-Emission Scanning Electron Microscope (FE-SEM, JSM-5600LV, JEOL, Japan). SEM imaging was employed to examine the morphology and size distribution of the ground powders.

EDX analyses were performed simultaneously with SEM imaging to check the elemental composition of the fine-milled powders at different stages of grinding and to follow possible contamination upon milling time.

2.3.3 Spectroscopic characterization

Chemical bonds were identified using Fourier transform infrared spectroscopy (FTIR) spectra collected in the 400–4000 cm^{-1} wavenumber range with an infrared Affinity-1 FTIR spectrometer (Shimadzu, Japan). The measurements were done on powdered samples prepared for transmission mode, enabling the detection of characteristic lattice vibrations, functional groups, and possible surface adsorbates [22–25].

2.3.4 Surface chemical analysis by X-ray photoelectron spectroscopy

XPS analysis of the $GeBi_2Te_4$ and $SnSb_2Te_4$ powders (Samples B and C) was carried out at the LSAM laboratory within the STAR Research Infrastructure at the University of Calabria (Italy), using a SPECS multichamber system operating under ultrahigh vacuum (UHV) conditions (base pressure $\approx 1 \times 10^{-9}$ mbar). The measurements were performed in normal emission conditions, with a PHOIBOS 100/150 hemispherical analyzer and a SPECS XR 50 M monochromatic Al Kα X-ray source ($h\nu = 1486.6$ eV). The core-level binding energies were calibrated with respect to the Fermi level, with an uncertainty of ± 0.02 eV.

Since the sample was in powder form, a small amount of $GeBi_2Te_4$ powder was dispersed in anhydrous solvent and drop-cast onto a thin Au(111) film epitaxially grown on mica to ensure electrical conductivity during the measurement. The same was done for $SnSb_2Te_4$ powders. The Au(111)/mica substrate was cleaned by several cycles of Ar^+ sputtering ($E = 1.5$ keV, $P = 3 \times 10^{-5}$ mbar) followed by annealing at 600 K. The cleanliness of the gold surface was verified through photoemission before the powder deposition.

2.3.5 Linear optical evaluations

Ultraviolet–Visible (UV–Vis) spectroscopic analysis was used to study the absorption characteristics of the nanostructured samples B and C. The linear optical absorption spectra were recorded using a Specord 210 Plus UV-Vis spectrophotometer (Analytic Jena, Germany), equipped with a deuterium–halogen light source. Measurements were carried out in the wavelength range of 190–700 nm using quartz cuvettes, where the powdered samples were dispersed in ethanol to ensure uniform light transmission. The obtained absorption data were analyzed using the Tauc [26–29] plots method for the estimation of the optical band gap (E_g). The Tauc formalism relates the absorption coefficient α to the photon energy $h\nu$ via the equation:

$$(\alpha h\nu) = A(h\nu - E_g)^n \tag{2}$$

where A is a constant, E_g is the optical band gap, and n depends on the nature of the electronic transition. Assuming an indirect allowed transition ($n = 2$), the optical band gap was determined by extrapolating the linear region of $(\alpha h\nu)^{1/2}$ vs. $h\nu$ plot to the energy axis.

3. Results and Discussion

3.1 Structural and morphological characterization of sample A

3.1.1 Structural evolution during milling

Figure 1 displays the PXRD patterns of hand-ground bulk $SnSb_2Te_4$ crystals (a), and samples subjected to HEBM for 5 h (b), 10 h (c), 15 h (d), and 20 h (e). $SnSb_2Te_4$ crystallizes in a trigonal structure with space group $R\bar{3}m$ and lattice

parameters $a = 4.3158$ Å and $c = 41.6574$ Å at ambient conditions [30, 31]. The PXRD patterns of the HEBM powders show significant broadening and intensity reduction of the basal peaks. As the milling time increases, the peaks continue to broaden slightly, indicating a reduction in crystallite size and a progressive disruption of the long-range order, particularly along the c-axis, where vdW forces weakly link the layers.

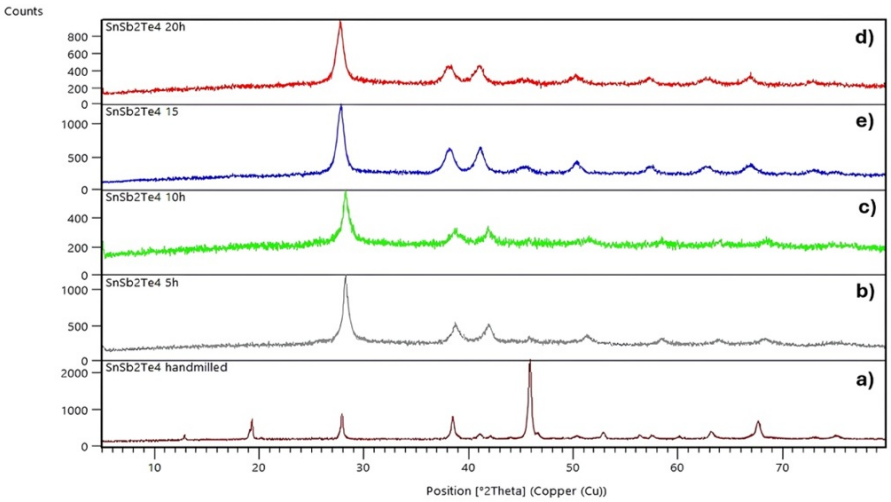

Figure 1. PXRD patterns of hand-milled $SnSb_2Te_4$ and HEBM powders (Sample A).

The average crystallite size of the powders was estimated using the Debye-Scherrer equation, and the corresponding values are summarized in Table 1. After 20 hours of milling, the average crystallite size was found to be approximately 9.35 nm, suggesting an approach toward the nanoscale. However, subsequent SEM results revealed a significant discrepancy: the actual particle size was found to be approximately 30 µm. This difference is related to the limitation of PXRD for determining particle size. It effectively tracks crystal domain size but does not accurately reflect the true particle size distribution. Therefore, using only crystallite size to judge milling efficiency can be misleading, especially when the goal is to produce nanoparticles.

Table 1.
Effect of milling time on crystallite and particle sizes of $SnSb_2Te_4$.

Milling Time (h)	FWHM	K	Average Crystallite Size (nm)	Average Particle size (µm)
Hand milled	0.218866	0.89	27.95	
5h	0.4948913	0.89	11.64	
10h	0.5805284	0.89	11.21	
15h	0.746415	0.89	9.65	
20h	0.7237008	0.89	9.35	30.34

3.1.2 SEM-EDX characterization

The morphological change of Sample A particles upon the milling time was followed via SEM imaging. Figure 2 shows the SEM micrographs of $SnSb_2Te_4$ particles after 20 h of milling under dry (upper panel, a) and ethanol-assisted (bottom panel, b) conditions. Significant differences in morphology are evident in the micrographs. Dry milling caused particle agglomeration and irregular shapes

(Figure 2a), while ethanol-assisted milling resulted in uniformly distributed particles (Figure 2b). This enhancement can be attributed to ethanol's dual role in facilitating exfoliation and minimizing particle re-agglomeration. Ethanol induces capillary forces that promote the cleavage of weakly bonded layers while also reducing interparticle friction.

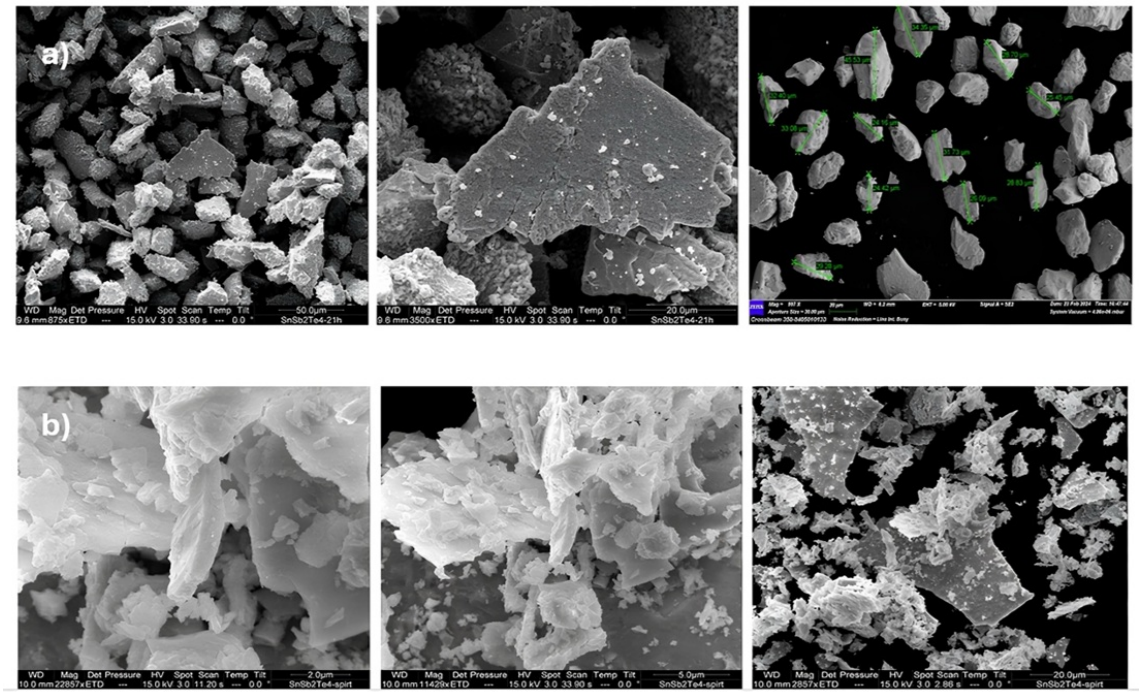

Figure 2. SEM micrographs of $SnSb_2Te_4$ (Sample A) particles after 20h of milling under dry (a, upper panel) and ethanol-assisted (b, bottom panel) conditions.

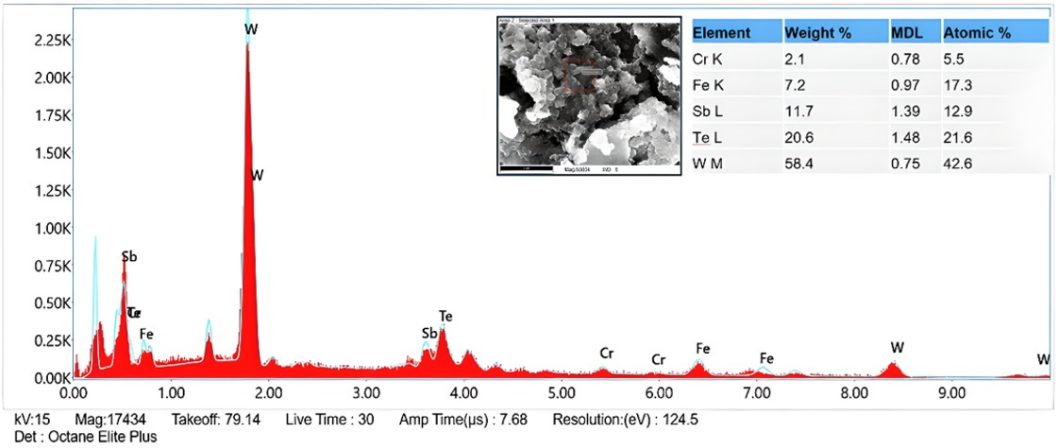

Figure 3. SEM-EDX data of Sample A milled for 20 h.

To test the potential contamination of the samples from the WC grinding vessel and balls, the EDX analysis was performed. As shown in Figure 3, the EDX spectrum of Sample A milled for 20 h revealed a significant level of tungsten contamination, exceeding 50 wt.%, indicating substantial wear of the vessel and balls. Such a high level of contamination not only masks the actual elemental composition of the target material but also complicates further structural and compositional analysis, particularly for techniques sensitive to matrix effects.

Given the increase in tungsten content upon the milling duration, further milling of Sample A was deemed unproductive, as the resulting material no longer reflected the intrinsic physical properties of $SnSb_2Te_4$. Consequently, nanoscale investigation under these conditions can be considered ineffective and irrelevant for practical applications of the elaborated material.

3.2 Structural and Morphological Characterization of Sample B

3.2.1 PXRD analysis

Figure 4 presents the PXRD patterns of the Sample B powders at different stages of the mechanical treatment: hand-milled (a), HEBM for 10 h (b), 20 h (c), and 40 h (d), respectively. The diffraction pattern of the hand-milled sample shows sharp, well-defined peaks that are in good agreement with literature data for the bulk $SnSb_2Te_4$ phase [5].

The diffraction peaks exhibit progressive broadening and intensity loss upon prolonged milling time. These changes reflect a gradual reduction in crystallinity and ordering, typically associated with lattice strain, defects, and structural distortion induced by HEBM. It is worth noting that no secondary phases or peak shifts were detected, even after 40 hours of milling, indicating that the ternary starting phase remains stable throughout the milling process.

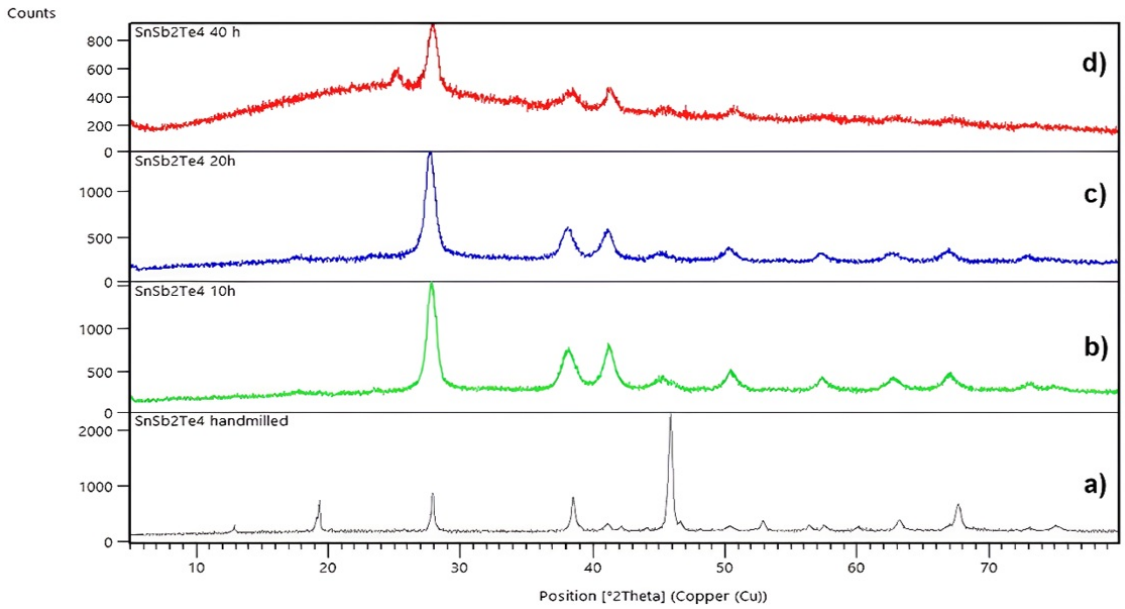

Figure 4. PXRD patterns of hand-milled $SnSb_2Te_4$ and HEBM powders (Sample B).

3.2.2 SEM-EDX characterization

Similar to XRD testing, SEM analysis was conducted on HEBM powders at various stages of milling. Figure 5(a) displays the SEM image of $SnSb_2Te_4$ powder after 40 hours of HEBM. As can be seen, the SEM micrograph reveals the formation of nanoflakes with irregular shapes and variable lateral dimensions. The corresponding particle size distribution derived from SEM image analysis

is presented in Figure 5(b), indicating an average particle size of approximately 65 nm with a relatively narrow distribution (SD ~ 6 nm). These results confirm the effective reduction of particle dimensions to the nanoscale.

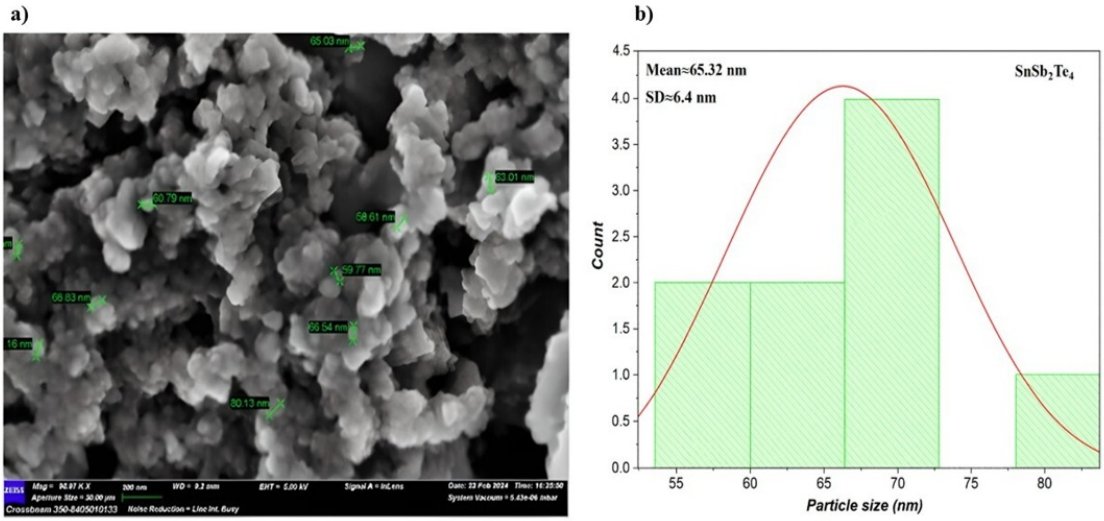

Figure 5. (a) SEM micrograph of $SnSb_2Te_4$ powder (Sample B) after 40 h of milling. (b) Particle size distribution derived from SEM analysis, revealing an average particle size of ~ 65 nm with a standard deviation of ~ 6 nm.

The EDX spectrum presented in Figure 6 confirms the elemental composition of the milled powder. A trace amount of contamination, approximately 0.7 wt.% Fe was detected, likely originating from the hardened steel vessel and balls. In comparison to Sample A, this is significantly lower and suggests that it is more suitable for the elaboration of pristine $SnSb_2Te_4$. These results emphasize the importance of the milling system's material in determining the outcome of mechanical milling. In the case of $SnSb_2Te_4$, no additives or surface protectants were used. By changing only the vessel and ball materials and optimizing the milling time, nanoscale refinement was achieved with minimal contamination. This approach provides a more controlled and efficient method for preparing nanoscaled ternary thermoelectric materials from bulk, keeping the starting composition. It also demonstrates effective contamination reduction through the selection of suitable vessel and ball materials and optimal milling variables.

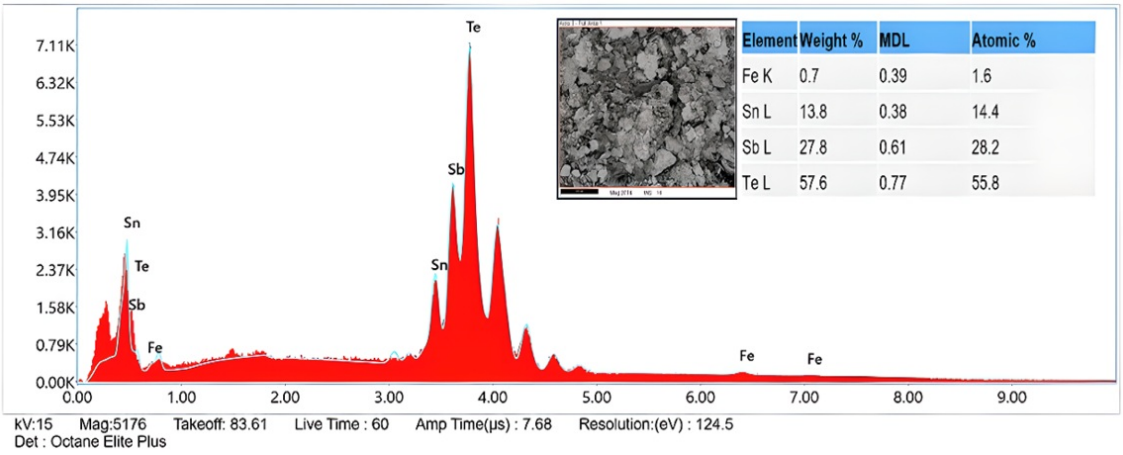

Figure 6. SEM-EDX data of Sample B after 40 h of milling, indicating a trace level (~ 0.7 wt.%) of contamination from hardened steel media.

The results obtained for Samples A and B demonstrate a remarkable contrast between the two materials. While Sample A was found to be contaminated by 50 wt.% tungsten after only 20 hours of milling, Sample B exhibited minimal contamination of just 0.7 wt.% Fe even after 40 hours. This dramatic improvement highlights the central role of the materials of the vessel and ball of the milling system in determining contamination sensitivity during HEBM. It shows that nanoscale refinement with minimal contamination can be achieved by changing grinding materials, without altering the target material or using protective agents. This outcome is particularly valuable for the preparation of pristine and nanoscale prospective thermoelectric materials based on layered vdW compounds.

3.2.3 Structural and phase purity analysis via FTIR spectroscopy

The FTIR spectrum of Sample B was measured in the range of 4000–500 cm^{-1} to identify the characteristic vibrational modes of the compound (Figure 7). A broad absorption band at 3438 cm^{-1} corresponds to O–H stretching vibrations, while the peak at 1617 cm^{-1} is attributed to H–O–H bending, both of which arise from surface-adsorbed moisture. The weak feature at 2363 cm^{-1} is assigned to atmospheric CO_2. In the low-frequency region, which is most significant for metal–chalcogenides, strong absorption bands appear at 673 cm^{-1} and 513 cm^{-1}, corresponding to Sn–Te and Te–M–Te lattice vibrations, respectively. These modes confirm the successful formation of the Sn–Sb–Te bonding network, in good agreement with reported data for related telluride compounds such as SnTe and Sb_2Te_3 [26,28]. The absence of additional sharp peaks indicates that no secondary oxide or organic impurity phases are present, suggesting good phase purity of the sample. Overall, the FTIR spectrum confirms the structural integrity of $SnSb_2Te_4$, while the minor O–H and CO_2 contributions are due to surface adsorption and do not affect the bulk material.

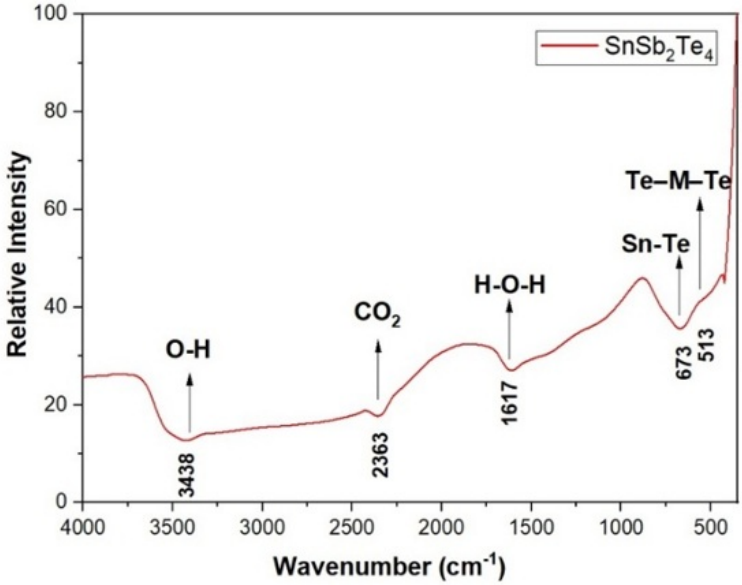

Figure 7. FTIR spectrum of $SnSb_2Te_4$ (Sample B) showing characteristic Sn–Te and Te–M–Te vibrations.

3.2.4 Surface elemental composition of $SnSb_2Te_4$

Figure 8 presents the XPS measurements for $SnSb_2Te_4$. The survey spectrum shows well-defined photoemission peaks, together with minor contributions from surface contaminants (oxygen and carbon) and from the Au(111) substrate used for powder deposition. In the Te 3d region, a clearly resolved spin–orbit doublet is observed, with an energy separation of approximately 10.3 eV between the $3d_{3/2}$ and $3d_{5/2}$ components – consistent with values reported for elemental tellurium and related chalcogenide compounds [30]. An additional TeO_2 component appears at higher binding energies relative to the main Te 3d peaks, indicating partial surface oxidation.

The Sn 3d peaks display a spin–orbit splitting of about 8.4 eV, in agreement with standard values reported for tin and tin-based compounds [31]. The Sb 3d spin–orbit doublet could not be resolved due to overlap with the Au 4p and O 1s peaks in the same spectral region.

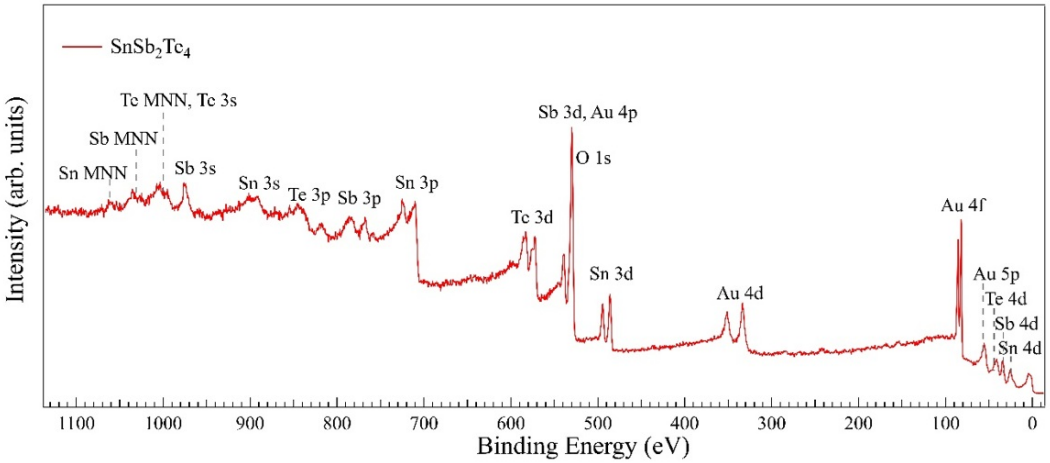

Figure 8. XPS survey spectrum of $SnSb_2Te_4$ powders deposited on Au(111) taken with a radiation source of Al K $\alpha_{1,2}$ 1486.61 eV.

3.2.5 UV–Vis absorption and band gap determination

The optical band gap of Sample B was obtained from UV–Vis absorption data using the Tauc method, where $(\alpha h\nu)^{1/2}$ was plotted against photon energy ($h\nu$) (Figure 9). This approach corresponds to an indirect allowed transition, where $n = 2$ in the Tauc relation. Extrapolating the linear region to the energy axis gave an estimated band gap of about 1.75 eV.

This value suggests that nanostructured $SnSb_2Te_4$ retains its indirect band gap character, in agreement with theoretical reports indicating that the valence-band maximum and conduction-band minimum are located at different k-points in the Brillouin zone [26]. The band gap falls within the visible range, making the newly elaborated material potentially suitable for optoelectronic and photovoltaic applications. However, it should be noted that the observed band gap value may not arise solely from quantum confinement effects. Contributions from surface oxidation and possible amorphization during the prolonged milling process may also influence the optical response. The relatively sharp absorption edge may

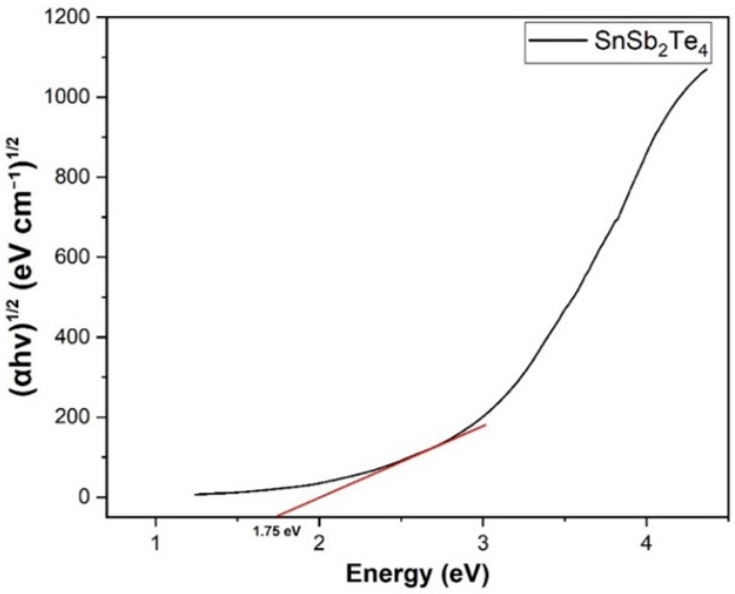

Figure 9. Tauc plots of the sample B assuming different indirect allowed transitions (n = 2).

indicate a certain degree of phase uniformity, in partial agreement with the FTIR results. Overall, while the moderate band gap suggests potential for thermoelectric and energy-conversion applications [30,32], a cautious interpretation is required due to possible surface and structural effects.

3.3 Structural and morphological characterization of sample C

3.3.1 SEM-EDX characterization

Similar to the $SnSb_2Te_4$ sample, SEM characterization was performed for Sample C after 40 h of milling. Figure 10(a) shows the SEM micrograph of $GeBi_2Te_4$ powder, revealing the formation of nanoflakes with irregular morphology and variable lateral dimensions. The corresponding particle size distribution derived from SEM image analysis is presented in Figure 10(b), indicating an average particle size of approximately 96 nm with a relatively broad distribution (SD ~ 18 nm). The corresponding EDX spectrum (Figure 11) confirms the elemental composition of the milled powder. Minor contamination was detected, with 2.4 wt.% Fe and 5 wt.% O, likely arising from the milling environment. These results verify the effective synthesis of nanosized $GeBi_2Te_4$ with minimal impurity incorporation.

3.3.2 Structural and phase purity analysis via FTIR spectroscopy

Figure 12 presents the FTIR spectrum of Sample C. The characteristic absorption bands observed at 474 and 638 cm^{-1} correspond to Ge–Te and Te–M–Te ($M = Ge/Bi$) vibrations, confirming the formation of the $GeBi_2Te_4$ compound. The bands at 1617 and 3438 cm^{-1} are associated with H–O–H bending and O–H stretching vibrations, respectively, indicating the presence of adsorbed moisture on the powder surface. A weak band at 2363 cm^{-1} is attributed to CO_2 absorption from the atmosphere. The spectrum confirms the successful synthesis of

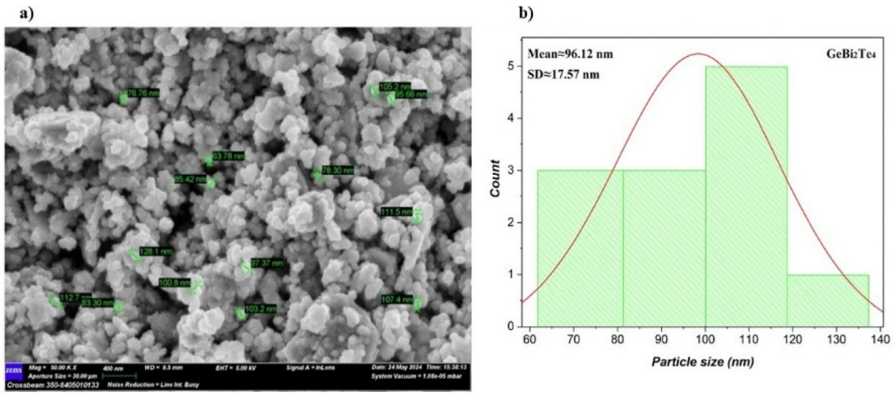

Figure 10. (a) SEM micrograph of $GeBi_2Te_4$ powder (Sample C) after 40 h of milling. (b) Particle size distribution derived from SEM analysis, revealing an average particle size of ~ 96 nm with a standard deviation of ~ 18 nm.).

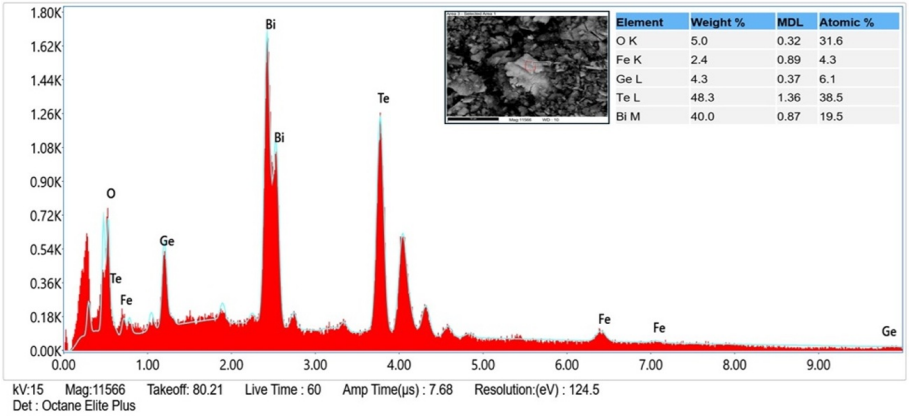

Figure 11. SEM-EDX data of Sample C after 40 h of milling, indicating a ~ 2.4 wt.% of contamination from hardened steel.

$GeBi_2Te_4$, with only minor surface oxidation and adsorption of moisture.

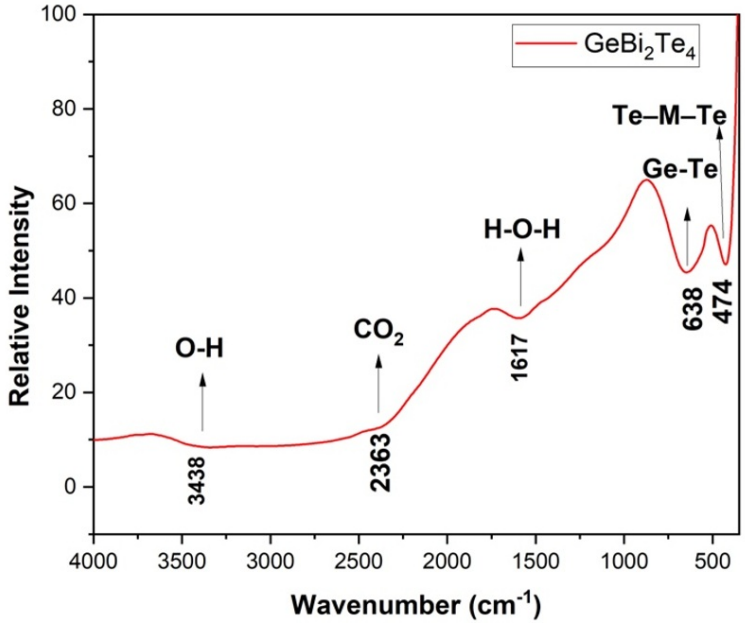

Figure 12. FTIR spectrum of $GeBi_2Te_4$ (Sample C) showing characteristic Ge–Te and Te–M–Te vibrations.

3.3.3 Surface elemental composition of $GeBi_2Te_4$

For $GeBi_2Te_4$, the XPS survey spectrum in Figure 13 also exhibits distinct photoemission peaks, with minor contributions from oxygen, carbon, and the underlying Au(111) substrate. The Te 3d region shows a well-defined spin–orbit doublet, with an energy separation of about 10.3 eV, matching the characteristic value for tellurium in similar chalcogenide systems [33].

The Bi 4f doublet presents a separation of approximately 5.4 eV between the $4f_{5/2}$ and $4f_{7/2}$ components, consistent with typical splittings observed in bismuth–telluride compounds and metallic bismuth [33]. The Ge 3p spin–orbit splitting could not be resolved under the present experimental conditions.

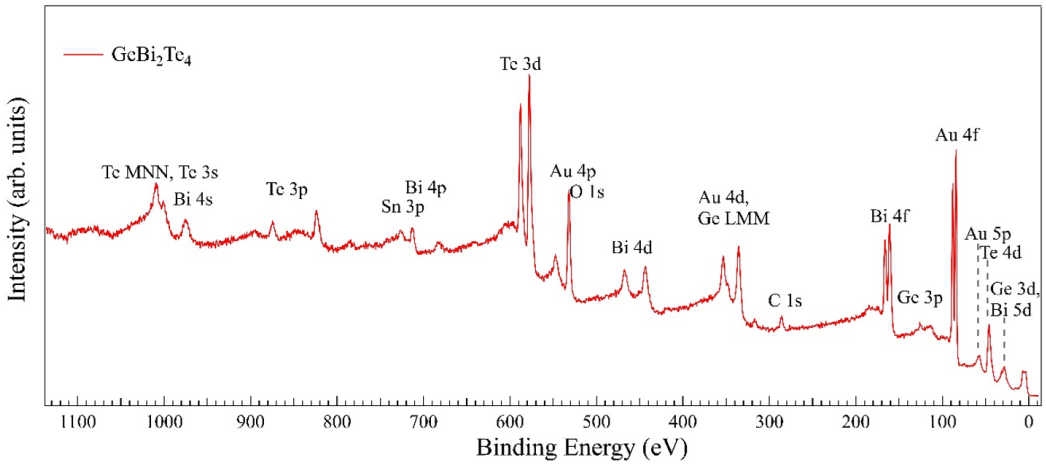

Figure 13. XPS survey spectrum of $GeBi_2Te_4$ powders deposited on Au(111) taken with a radiation source of Al K $\alpha_{1,2}$ 1486.61 eV.

3.3.4 UV–Vis absorption and band gap determination

Figure 14 presents the Tauc plot of the milled $GeBi_2Te_4$ powder. The optical band gap, determined by extrapolating the linear portion of the $(\alpha h\nu)^2$ versus $h\nu$ curve, is estimated to be 1.58 eV. This analysis assumes a direct allowed transition, consistent with previous electronic-structure studies reporting a direct band gap at the Γ point for bulk $GeBi_2Te_4$ [34].

Similar to the $SnSb_2Te_4$ sample discussed above, the significantly larger band gap value observed here is unlikely to arise solely from size-induced quantum confinement. As mentioned above, additional contributions from surface oxidation, possible structural disorder, or amorphous phases formed during the prolonged milling process may also affect the optical response. Therefore, the obtained band gap should be interpreted carefully, as it likely reflects a combination of effects rather than the intrinsic property of the crystalline phase.

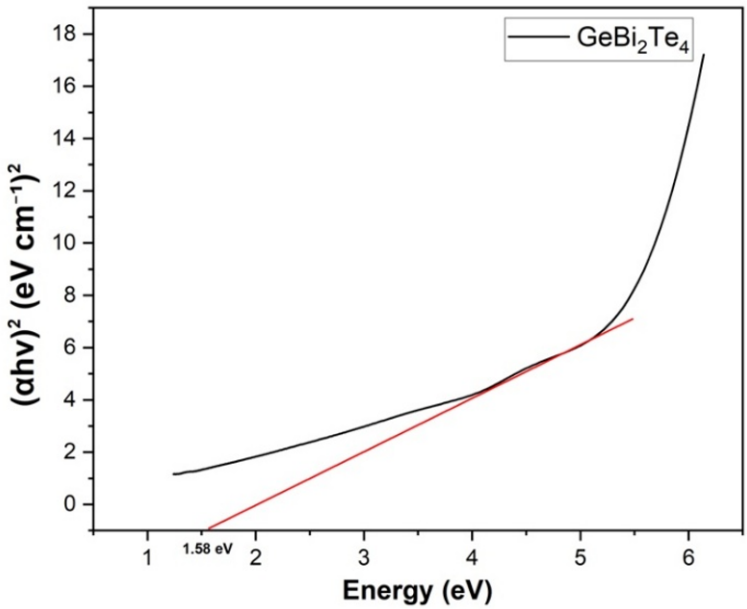

Figure 14. Tauc plots of the Sample C assuming different indirect allowed transitions.

Conclusion

In this study, nanostructured $SnSb_2Te_4$ and $GeBi_2Te_4$ were successfully prepared from single-crystal ingots using high-energy ball milling. The results demonstrate that the choice of milling media strongly influences sample purity. It was confirmed that the tungsten carbide bowl and balls leads to significant contamination, whereas the stainless-steel milling system considerably reduces impurities while enabling effective nanoscale refinement.

PXRD and SEM-EDX analyses confirm that HEBM reduces particle size to the nanometer range, while FTIR and UV–Vis measurements provide insight into the structural and optical properties of the processed powders. The optical band gaps were estimated to be $\sim$ 1.75 eV for $SnSb_2Te_4$ and $\sim$ 1.58 eV for $GeBi_2Te_4$. However, as discussed above, these values are significantly larger than bulk counterparts and may be influenced not only by size reduction but also by surface oxidation, structural disorder, and possible amorphization induced during prolonged milling.

XPS measurements further confirm the presence of the constituent elements and stoichiometry, with minor contributions from surface oxidation and the Au substrate.

Overall, these results indicate that HEBM is a simple and scalable approach for producing nanosized van der Waals thermoelectric materials. While the obtained powders exhibit low contamination levels and modified optical responses, further studies are required to fully understand the origin of the observed band gap values and their relationship to structural and surface effects.

Acknowledgement

This research was partially supported by "Progetto STAR 2" (PIR01-00008) of the Italian Ministry of Education, University, and Research (MUR).

References

[1] G.J. Snyder, E.S. Toberer, Nature Materials **7** (2008) 105–114. [*CrossRef*]
[2] C.J. Vineis et al., Advanced Materials **22** (2010) 3970–3980. [*CrossRef*]
[3] D.M. Rowe, Thermoelectric Handbook: Macro to Nano. CRC Press/Taylor & Francis (2006). [*CrossRef*]
[4] S. Zachariah, I. Ravanan, Journal of Alloys and Compounds **1043** (2025) 184187. [*CrossRef*]
[5] G. Wang et al., Ceramics International **50** (2024) 25771–25778. [*CrossRef*]
[6] J. Dong et al., Advanced Functional Materials **34** (2024) 2314499. [*CrossRef*]
[7] L.D. Hicks, M.S. Dresselhaus, Physical Review B **47** (1993) 12727–12731. [*CrossRef*]
[8] M.S. Dresselhaus et al., Advanced Materials **19** (2007) 1043–1053. [*CrossRef*]
[9] B. Poudel et al., Science **320** (2008) 634–638. [*CrossRef*]
[10] Y. Ma et al., Nano Letters **8** (2008) 2580–2584. [*CrossRef*]
[11] D. Kim et al., Journal of Alloys and Compounds **509** (2011) 5211–5215. [*CrossRef*]
[12] W.J. Xie et al., Nano Letters **10** (2010) 3283–3289. [*CrossRef*]
[13] J.L. Wu et al., Journal of Alloys and Compounds **509** (2011) 2116–2126. [*CrossRef*]
[14] J.R. Szczech, J.M. Higgins, S. Jin, J. Mater. Chem. **21** (2011) 4037–4055. [*CrossRef*]
[15] D. Dhak, P. Pramanik, Journal of the American Ceramic Society **89** (2006) 534–547. [*CrossRef*]
[16] J.F. Li et al., NPG Asia Materials **2** (2010) 152–158. [*CrossRef*]
[17] A.I. Hochbaum et al., Nature **451** (2008) 163–167. [*CrossRef*]
[18] Y. Wang et al., Progress in Materials Science **156** (2026) 101575. [*CrossRef*]
[19] H.J. Goldsmid, Materials **7** (2014) 2577–2592. [*CrossRef*]
[20] Z.S. Aliev et al., J. Mater. Sci.: Mater. Electron. **37** (2026) 282. [*CrossRef*]
[21] D. Zang et al., Materials **18** (2025) 2494. [*CrossRef*]
[22] Y. Xu, N. Al-Salim, J.M. Hodgkiss, R.D. Tilley, Crystal Growth & Design **11** (2011) 2721–2725. [*CrossRef*]
[23] S. Khosravi Gandomani, B. Khoshnevisan, R. Yousefi, Journal of Luminescence **203** (2018) 485–485. [*CrossRef*]
[24] J. Tauc, R. Grigorovici, A. Vancu, physica status solidi (b) **15** (1966) 627–637. [*CrossRef*]
[25] E.A. Davis, N.F. Mott, Philosophical Magazine **22** (1970) 903–922. [*CrossRef*]
[26] Y. Zhang et al., Nanoscale Advances **2** (2020) 1333–1339. [*CrossRef*]
[27] P. Makula, M. Pacia, W. Macyk, The Journal of Physical Chemistry Letters **9** (2018) 6814–6817. [*CrossRef*]

[28] M. Adam, J. Alloys Compd. **765** (2018) 1072–1081. [*CrossRef*]
[29] M. Adam et al., Superlattices and Microstructures **155** (2021) 106909. [*CrossRef*]
[30] T.V. Menshchikova, S.V. Eremeev, E.V. Chulkov, Appl. Surf. Sci. **267** (2013) 1–3. [*CrossRef*]
[31] Thermo Fisher Scientific, Tin (Sn) XPS spectra and chemical states, online document (2025).[*Web Link*]
[32] H. Wu, P. Chen, Z. Zhou, et al., J. Mater. Sci. Technol. **154** (2023) 140–148. [*CrossRef*]
[33] J.H. Guo et al., Chinese Physics Letters **30** (2013) 106801. [*CrossRef*]
[34] D. Marcinkova et al., Phys. Rev. B **88** (2013) 165128. [*CrossRef*]